

Mode-locked laser in nanophotonic lithium niobate

Qiushi Guo^{1,2,3†}, Ryoto Sekine¹, James A. Williams¹, Benjamin K. Gutierrez⁴, Robert M. Gray¹, Luis Ledezma^{1,5}, Luis Costa¹, Arkadev Roy¹, Selina Zhou¹, Mingchen Liu¹, Alireza Marandi^{1†}

¹*Department of Electrical Engineering, California Institute of Technology, Pasadena, CA, USA*

²*Photonics Initiative, Advanced Science Research Center, City University of New York, NY, USA*

³*Physics Program, Graduate Center, City University of New York, New York, NY, USA*

⁴*Department of Applied Physics, California Institute of Technology, Pasadena, CA, USA*

⁵*Jet Propulsion Laboratory, Pasadena, CA, USA*

†Email: qguo@gc.cuny.edu; marandi@caltech.edu

(Dated: August 31, 2024)

Mode-locked lasers (MLLs) have enabled ultrafast sciences and technologies by generating ultra-short pulses with peak powers substantially exceeding their average powers. Recently, tremendous efforts have been focused on realizing integrated MLLs not only to address the challenges associated with their size and power demand, but also to enable transforming the ultrafast technologies into nanophotonic chips, and ultimately to unlock their potential for a plethora of applications. However, till now the prospect of integrated MLLs driving ultrafast nanophotonic circuits has remained elusive because of their typically low peak powers, lack of controllability, and challenges with integration with appropriate nanophotonic platforms. Here, we overcome these limitations by demonstrating an electrically-pumped actively MLL in nanophotonic lithium niobate based on its hybrid integration with a III-V semiconductor optical amplifier. Our MLL generates ~ 4.8 ps optical pulses around 1065 nm at a repetition rate of ~ 10 GHz, with pulse energy exceeding 2.6 pJ and a high peak power beyond 0.5 W. We show that both the repetition rate and the carrier-envelope-offset of the resulting frequency comb can be flexibly controlled in a wide range using the RF driving frequency and the pump current, paving the way for fully-stabilized on-chip frequency combs in nanophotonics. Our work marks an important step toward fully-integrated nonlinear and ultrafast photonic systems in nanophotonic lithium niobate.

Mode-locked lasers (MLLs), which generate intense and coherent ultrashort optical pulses on picosecond and femtosecond timescales, have enabled numerous sciences and technologies in photonics such as extreme nonlinear optics¹, femtochemistry², supercontinuum generation³, optical atomic clocks^{4,5}, optical frequency combs⁶, biological imaging^{7,8}, and photonic computing⁹. Today's state-of-the-art MLLs are based on discrete fiber-based and free-space optical components and are expensive, power-demanding, and bulky. Realizing MLLs on integrated photonic platforms promises widespread utilization of ultrafast photonic systems which are currently limited to table-top laboratory experiments. However, so far the performance of integrated MLLs has not been on par with their table-top counterparts, lacking the required peak intensities and degrees of controllability required for on-chip ultrafast optical systems¹⁰, and many of the high-performance MLLs are not yet integratable with nanophotonic platforms. A major challenge lies in the simultaneous realization of large laser gain and an efficient mode-locking mechanism on integrated photonic platforms. Although III-V semiconductor gain media can be electrically pumped and they generally exhibit a very high gain per unit length and high saturation powers¹¹, the conventional method of achieving mode-locking and short pulse generation on the same semiconductor chip requires a narrow range of pumping current, thus significantly limiting the output power and the tunability of the integrated MLLs^{12–14}.

To realize high-peak-power integrated MLLs, a promis-

ing approach consists of the hybrid integration of a semiconductor gain medium and an external mode-locking element based on electro-optic (EO) or nonlinear optical effects. Recently, thin-film lithium niobate (TFLN) has emerged as a promising integrated nonlinear photonic platform with access to power-efficient and high-speed EO modulation^{15,16} and strong quadratic ($\chi^{(2)}$) optical nonlinearity^{17,18}. Hybrid integration of semiconductor gain with TFLN enables a strong interplay between the laser gain and the EO or nonlinear effects to achieve active or passive mode-locking with high efficiency and tunability. Moreover, many of the nonlinear and ultrafast optical functionalities such as supercontinuum generation¹⁹, optical parametric oscillation^{20–23}, pulse shortening²⁴, all-optical switching²⁵, and quantum squeezing²⁶ can be realized in quasi-phase-matched LN nanophotonic devices with orders of magnitude lower peak powers compared to other platforms. Therefore, developing high-peak-power MLLs integrated into nanophotonic LN can enable a suite of nonlinear and ultrafast optical phenomena on a chip, promising integrated photonic systems with unprecedented performance and functionalities.

In this work, we demonstrate a high-peak-power, electrically-pumped integrated actively MLL by hybrid integration of III-V semiconductors and LN nanophotonics. In contrast to conventional integrated MLLs based on hybrid integration of a III-V active region and a passive waveguide^{10,12}, our MLL synergistically exploits the high laser gain of III-V semiconductors and the ef-

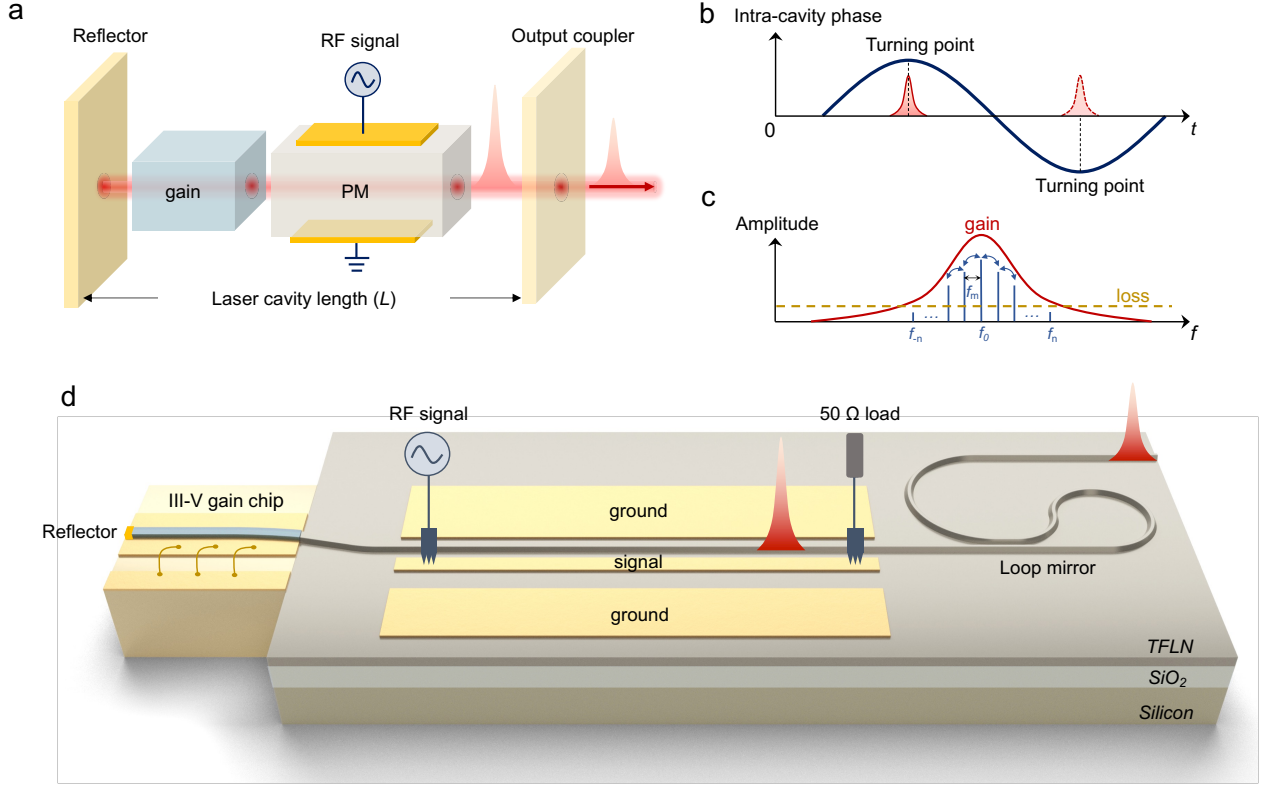


FIG. 1. **Principle and design of integrated actively MLL laser** **a**, Concept of active mode-locking through intra-cavity phase modulation. **b**, Illustration of mode-locking in the time domain. **c**, Illustration of mode-locking in the frequency domain. **d**, Schematic of the integrated actively MLL. The laser is composed of a single-angled facet (SAF) gain chip butt-coupled to a TFLN chip, which is composed of an electro-optic phase modulator and a broadband loop mirror.

ficient active optical phase modulation in LN nanophotonic waveguides as the mode-locking mechanism. Such a design eliminates the complexities associated with realizing gain and saturable absorption on the same semiconductor chip, allowing a much higher output power and a wider tunability of the laser. Under an external RF drive of less than 300 mW, our MLL generates ultrashort optical pulses around 1065 nm with a pulse duration of approximately 5 ps, pulse energy greater than 5 pJ, and a peak power greater than 0.5 W. This represents the highest reported peak power at a repetition rate of ~ 10 GHz for integrated MLLs in nanophotonics. The MLL can operate over a broad range of electrical pumping currents and RF driving frequencies, and provide precise control of the carrier frequency and repetition rate of the resulting frequency comb, which can lead to fully-stabilized comb sources. In contrast to other recent demonstrations of ultrashort pulse sources on the TFLN platform such as Kerr soliton micro-combs^{27,28} and electro-optic (EO) combs^{29–31}, our MLL provides significantly higher on-chip peak power and pulse energies, and electrical-to-short-pulse efficiencies. Moreover, our MLL offers great system simplicity by eliminating the need for wavelength-tunable pump lasers, external opti-

cal amplification stages, complex cavity locking schemes, and/or pulse compression elements with high optical loss. The simplicity of our MLL design, combined with its high peak power, few-picosecond pulses, and controllable frequency comb parameters offers a practical path for fully-integrated nonlinear and ultrafast photonic systems in LN nanophotonics.

Operating principle and design of the MLL:

Figure 1a shows the concept of active mode-locking by electro-optic phase modulation inside a laser cavity. In the time domain, when a phase modulator (PM) is driven by a sinusoidal RF signal at a frequency f_m , the intra-cavity phase modulation is equivalent to the cavity length modulation. Therefore, the laser cavity can be considered as having a moving end mirror with a sinusoidal motion at frequency f_m . When an optical signal inside the cavity strikes this moving end mirror and gets reflected back, its optical frequency acquires a Doppler shift. After successive round trips, these Doppler shifts will accumulate, resulting in no steady-state solution. However, when a short circulating pulse strikes the end mirror at either of the “turning points” where the mirror reverses its direction (the extremum of the phase variation as shown in Fig. 1b), it will not acquire a Doppler frequency shift but

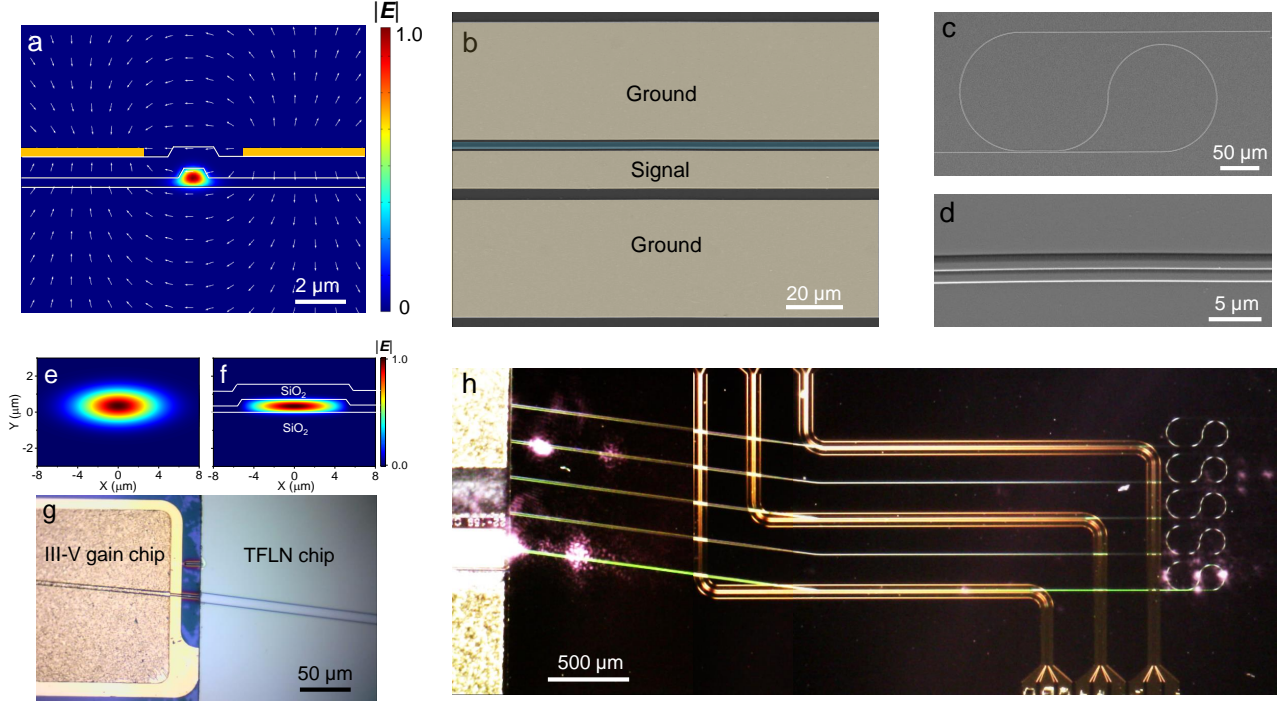


FIG. 2. **Integrated actively MLL laser on TFLN.** **a**, Cross-sectional view of the phase modulator (PM) region and the distribution of microwave field (white arrows) at 10 GHz and the optical field of the fundamental TE mode (color map) at 1065 nm. The top width of the TFLN waveguide is 800 nm. The gap between the signal and the ground electrodes is designed to be $4\ \mu\text{m}$. The RF electrodes are marked in yellow. **b**, False-colored scanning electron microscope (SEM) image of the PM region in the fabricated device. The RF electrodes are marked in yellow and the optical waveguide is marked in blue. The remaining dark grey regions are the etched TFLN slab. **c**, SEM image of the broadband loop mirror. **d**, Zoom-in view of the curved coupling region of the broadband loop mirror. **e**, Fundamental TE mode profile at 1065 nm in the SAF gain chip waveguide. **f**, Fundamental TE mode profile at 1065 nm in the TFLN waveguide taper. **g**, Optical microscope image showing the coupling region between the two chips. **h**, Dark-field optical microscope image of the integrated actively MLL when operating.

instead a small quadratic phase modulation or chirp^{31,32}. Thus, an optical pulse can be maintained in the laser cavity after successive round trips as a steady-state solution. The characteristics of the pulse depend on the gain, loss, and dispersion in the cavity as well as the chirp from the PM. While in principle optical pulses can occur at either of the two phase modulation extrema and acquire chirp of different signs, the dispersion in the cavity can compensate for the chirp imposed by the PM at one extremum, and further chirp the pulse formed at another extremum. As a result, the combination of dispersion, gain, and nonlinear effect in the cavity can favor one pulse over the other, leading to only one pulse in the cavity³³. Such a mode-locking condition necessitates a good match between the phase modulation time period and the cavity round-trip time (f_m should be close to the cavity free spectral range (FSR)). The mode-locking mechanism can also be understood in the frequency domain. As shown in Fig. 1c, if the intra-cavity phase modulation frequency f_m matches the cavity FSR, the sidebands produced by each of the running axial modes are injected into the adjacent axial modes, resulting in the phase locking of adjacent modes. While the mutual

injection of spectral modes within the cavity bears similarity to EO comb sources, it is important to note that in MLLs, these modes will lase due to the presence of laser gain within the cavity, whereas in EO comb sources, they are generated by dispersing the energy from a single pump laser line^{29–31,34}. This distinction gives rise to stark differences in their operations.

Based on this principle, we design the integrated actively MLL as shown in Figure 1c. In our MLL, an electrically pumped gain section based on a single-angled facet GaAs gain chip (SAF gain chip) is butt-coupled to a TFLN chip, which contains an integrated EO phase modulator (PM) and a broadband loop mirror. A Fabry-Perot laser cavity configuration is formed between the reflective facet on the left end of the SAF gain chip and the broadband loop mirror on the TFLN chip. Here, an integrated PM is preferred over a Mach Zehnder interferometer (MZI)-based intensity modulator (IM) because the PM offers a lower insertion loss and avoids effects from the DC bias drift of the MZI modulator³⁵. Thus, our MLL principle is distinct from that of an actively MLL based on an IM, in which the mode-locking is enabled by loss modulation³⁶. It is worth noting that semiconductor

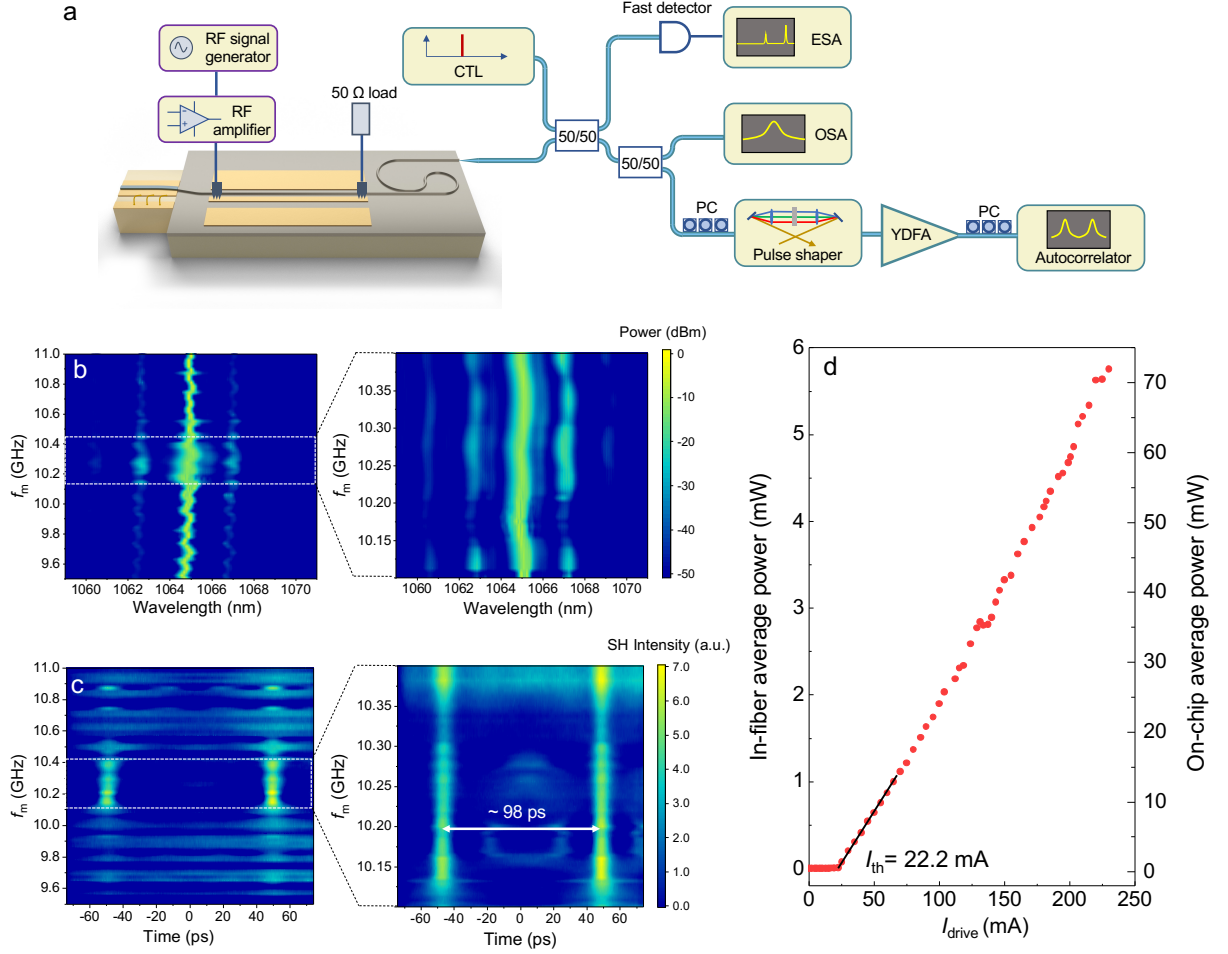


FIG. 3. Characterization of integrated actively MLL and its operating regimes **a**, Schematic of the setup for characterizing integrated actively MLL. The laser output from the waveguide facet was collected by a lensed fiber. In the measurement, we simultaneously monitored the optical spectrum from the optical spectrum analyzer (OSA), the intensity autocorrelation, and the heterodyne beatnote of the laser output. Heterodyne beat note was measured using a reference continuously tunable CW laser (Toptica CTL) operating around 1065 nm, a fast photodetector (FPD), and an electrical spectrum analyzer (ESA). **b**, The optical spectrum of the MLL output as a function of the RF driving frequency (f_m). Significant spectrum broadening is found when f_m is between 10.1 and 10.4 GHz. **c**, Intensity autocorrelation of the MLL output as a function of the f_m . Two distinct intensity autocorrelation peaks separated by ~ 98 ps emerged when f_m is tuned to be between 10.1 and 10.4 GHz. **d**, Dependence of laser average output power on the driving current (I_{drive}) when $f_m = 10.17$ GHz.

gain medium typically has a short carrier relaxation time (gain recovery time (T_G)) on the order of ns^{11,36,37}. To ensure the mode-locking and the formation of ultrashort optical pulses, T_G has to exceed the cavity round-trip time (T_{RT}) of pulses by a large amount ($T_G \gg T_{\text{RT}}$)³⁶. In our design, by controlling the length of the TFLN waveguide, we realized this condition by having a cavity FSR of ~ 10 GHz, which translates to a cavity round-trip time of ~ 100 ps.

We fabricated our devices on a 700-nm-thick X-cut magnesium-oxide (MgO) doped TFLN on a SiO₂/Silicon (4.7 $\mu\text{m}/500$ μm) substrate (NANOLN). The details about the device fabrication can be found in the Methods. As shown in Fig. 2a, in the PM region, the RF electrodes

are fabricated on top of the SiO₂ cladding layer. Such a design allows us to achieve high modulation efficiency (simulated value of 1.1 V \cdot cm) by having a small gap (4 μm here) between the ground and signal electrodes and a significant overlap between the RF field and the optical field in the waveguide^{16,38}. It also ensures a low optical propagation loss by offering a high tolerance to misalignment between the electrodes and the optical waveguide¹⁶. We designed the geometry of the RF electrode to ensure a 50 Ω impedance around 10 GHz. Figures 2b, c, and d show the scanning electron microscope (SEM) images of the PM and the loop mirror regions of the fabricated device. In the loop mirror, we adopted a curved coupling region design³⁹ which increases the reflective band-

width. The detailed design of the broadband loop mirror is described in the Supplementary Information Section II. Based on the length (1.5 mm) and the refractive index of the SAF gain chip around 1065 nm, we estimate that a ~ 3 -mm-long TFLN waveguide can lead to a laser cavity FSR of ~ 10 GHz.

Figure 2e shows the 1065-nm fundamental TE mode profile in the waveguide of the SAF gain chip, which is calculated from the divergence angle of its emission. To minimize the coupling loss between the SAF gain chip and the TFLN chip, the top width of the input facet of the TFLN waveguide is tapered out to be $10.3 \mu\text{m}$. The 1065-nm fundamental TE mode profile in the tapered TFLN waveguide is shown in Fig. 2f. This design ensures a maximal overlap with the optical mode produced by the SAF gain chip and yields a minimal coupling loss of ~ 1.5 dB. In Section I of the Supplementary Information, we discuss the dependence of coupling loss on the lateral misalignment and gap between the SAF gain chip and TFLN waveguides. The coupling loss can be further reduced by employing a polymer-based mode-size converter⁴⁰. Fig. 2g shows the microscope image of the coupling region after the alignment, in which the gap between the two chips is minimized. When the SAF gain chip is electrically pumped with a driving current (I_{drive}) of 160 mA, we observe green light (the second harmonic of the 1065 nm light) inside the laser cavity (Fig. 1h), which indicates a high intra-cavity power around 1065 nm and a good alignment between the two chips.

Characterization of the MLL: We characterized the integrated actively MLL using an optical setup shown in Fig. 3a. We applied a ~ 280 mW sinusoidal RF signal to the left end of the traveling wave electrodes (TWE) of the PM by the RF probe. The right end of the TWE is terminated by another RF probe with a 50Ω load resistor mounted on it. To investigate the operating regimes of the MLL, we simultaneously collect the laser output spectra, the intensity autocorrelation of the laser output in the time domain, and the heterodyne beat notes between two neighboring laser emission lines and a narrow-linewidth (~ 10 kHz) reference CW tunable laser (CTL, Toptica). In order to get intensity autocorrelation with a good signal-to-noise ratio, we pre-amplified the laser output power by a Ytterbium-doped fiber amplifier (YDFA). We also used a pulse shaper (Waveshaper 1000A, II-VI) to compensate for the group velocity dispersion (GVD) imposed by the phase modulator, YDFA, and the single-mode fiber. In the measurement, the gain chip is electrically pumped with an I_{drive} of 185.2 mA.

As shown in Fig. 3b, when we widely scan the f_m , the laser output exhibits a clear spectral broadening when f_m is between 10.1 and 10.4 GHz (labeled by the white dashed box). Meanwhile, within this f_m range, two distinct intensity autocorrelation peaks separated by ~ 98 ps emerge (Fig. 3c), which indicates that optical pulses are formed in this f_m regime. At a f_m of 10.17 GHz, we measured the laser output power from the output facet of the TFLN chip with a single-mode lensed fiber. As

shown in Fig. 3d, the laser exhibits a very low threshold I_{drive} of 22 mA. Given the measured coupling loss of ~ 11 dB between the TFLN waveguide and the single-mode lensed fiber, the on-chip laser output average power is more than 50 mW when the I_{drive} is greater than 180 mA.

We further use the heterodyne beat notes to characterize the mode-locking and the resulting frequency comb. As illustrated in Fig. 4a, when the frequency of the reference CTL is resting in between the two neighboring comb lines of the MLL near the center of its spectrum, two RF beat notes at f_1 and f_2 are generated on the fast detector. Figure 4b shows the evolution of heterodyne beat notes as a function of f_m . When f_m is between 10.165 and 10.173 GHz as labeled by the white dashed box, two spectrally narrow beat notes are observed. This suggests that within this range of f_m , the laser is operating in the mode-locked regime so that neighboring axial modes of the laser are phase-locked and it produces a frequency comb with narrow spectral peaks. In the time domain, this means a good synchronization between the round-trip of the pulse in the cavity and the phase modulation has been achieved, and the laser produces ultrashort optical pulses with high coherence.

We also want to comment on some of the important behaviors of the resulting frequency comb when f_m is detuned from the cavity FSR. First, when the detuning is small ($10.165 \text{ GHz} < f_m < 10.173 \text{ GHz}$), we can still get two narrow beat notes, but f_1 and f_2 can shift significantly with f_m , as shown in Fig. 4b. This indicates that the carrier frequency of the MLL sensitively depends on f_m . Second, when the f_m is further detuned from the cavity FSR, the MLL exhibits a transition to a turbulent regime⁴¹, which is manifested by multiple noisy beat notes around f_1 and f_2 in Fig. 4b. In the turbulent regime, the MLL can no longer reach steady state. In this regime, the laser can still emit ultrashort pulses as shown in Fig. 3c, albeit with low coherence.

As shown in Fig. 4c, at $f_m = 10.17$ GHz, we obtained two spectrally narrow RF beat notes at $f_1 = 3.68$ GHz and $f_2 = 6.49$ GHz, with a full width at half maximum (FWHM) linewidth of 3.95 MHz and 3.91 MHz, respectively. Given that the RF drive has a very small phase noise and no active locking of the laser cavity is used here, the linewidths of the heterodyne beat notes can be mainly limited by the drift of pulse carrier frequency. As shown in Fig. 4d, when a 280 mW RF drive at 10.17 GHz is applied to the PM, significant spectral broadening is observed. The pulse spectrum is centered at 1064.9 nm and the FWHM of the spectrum is 0.35 nm. Meanwhile, we also collected the intensity autocorrelation of the MLL output at $f_m = 10.17$ GHz, as shown in Fig. 4e. The autocorrelation trace indicates that the MLL produces one strong pulse at one of the modulation turning points, while the other pulse is significantly suppressed. The Gaussian fit of the intensity autocorrelation trace yields a pulse width of 4.81 ps (5.03 ps) with (without) the external pulse shaping. Since the pulse

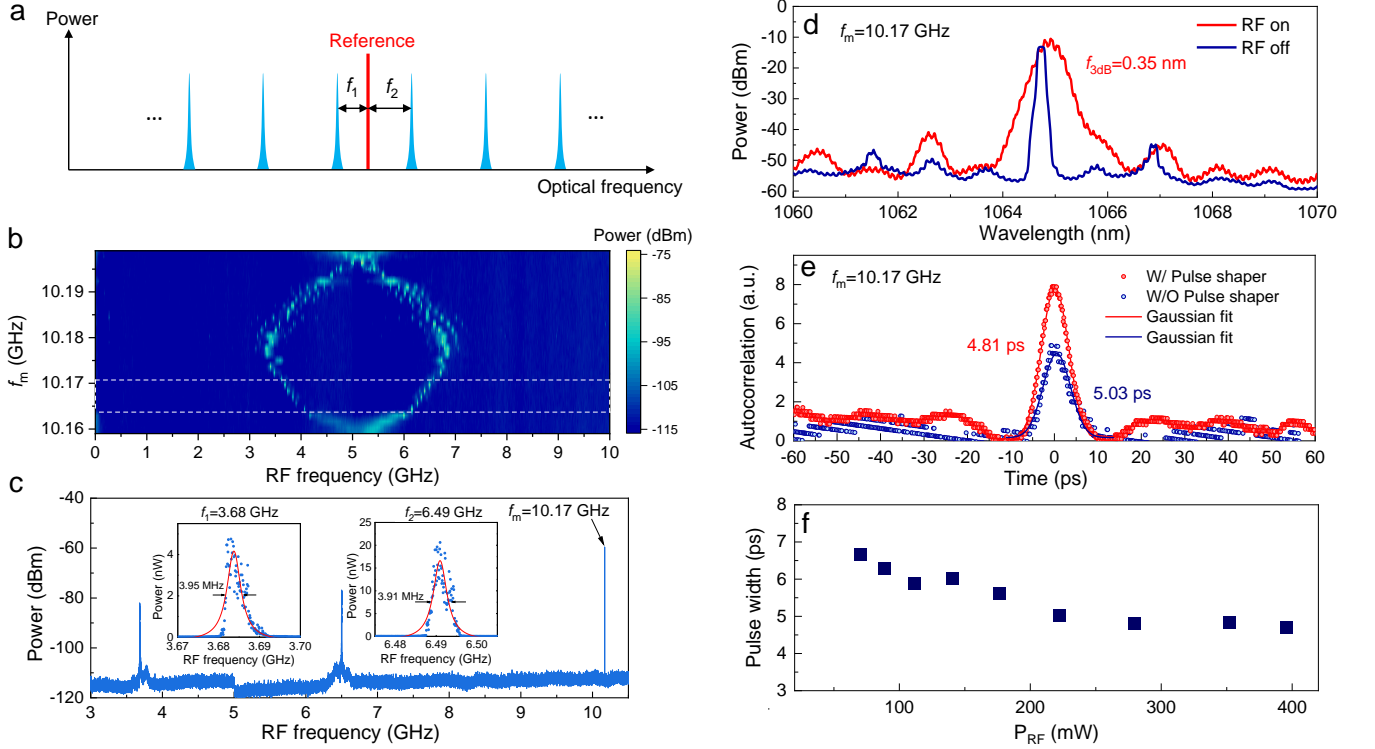


FIG. 4. **Finding the mode-locking regime of integrated actively MLL** **a**, Illustration of heterodyne beat notes generation. When the reference CTL frequency is between the two longitudinal mode frequencies of the MLL output near the center of its spectrum, two beat notes at RF frequencies of f_1 and f_2 will be detected by a fast detector **b**, Evolution of heterodyne beat notes with the f_m . The mode-locking regime is marked by the white dashed box. **c**, Heterodyne beat notes measured at $f_m = 10.17$ GHz. Insets: zoom-in view of the two beat notes at $f_1 = 3.68$ GHz and $f_2 = 6.49$ GHz. Blue symbols are measured data and solid red curves are Lorentz fits. **d**, Output optical spectra of the MLL when the RF drive at 10.17 GHz is on (red) and off (blue). **e**, Intensity autocorrelation traces of the MLL output measured at $f_m = 10.17$ GHz with (red) and without (blue) the external pulse shaper. Symbols are measurement data and solid curves are Gaussian fits. **f**, Dependence of pulse width on the RF driving power (P_{RF}).

shaper can compensate for the chirp on the output pulse and the additional chirp imposed by the SMF and the YDFA, we expect the output pulse width directly after the MLL facet to be between 4.81 ps and 5.03 ps. The pulse width of 4.81 ps after pulse shaping corresponds to a time-bandwidth product of 0.445, which is very close to the transform-limited time-bandwidth product (0.44) of a Gaussian pulse⁴². To conservatively estimate the pulse energy and peak power, we use the measured output average power of 53 mW at $I_{drive} = 185.2$ mA and assume both pulses exist in the cavity. Hence, the output pulse energy of our MLL is at least 2.6 pJ and the pulse peak power is greater than 0.51 W.

We further studied the limits of the output pulse width of our MLL. First, we measured how the pulse width changes with the RF power (P_{RF}) applied to the PM. As shown in Fig. 4f, the measured pulse only slightly decreases with increasing P_{RF} , which is in good agreement with the power scaling law according to the Haus Master Equation (HME)⁴³. We also found that further increasing the RF power will not shorten the pulse significantly. Instead, it can lead to laser instability due

to index modulation of the TFLN waveguide caused by RF heating. By using the HME and ignoring the GVD and nonlinear effects in the laser cavity, we estimate that the pulse width limit of our actively MLL is ~ 2.3 ps (see Supplementary Information Section IV for details). The experimentally measured pulse width is wider likely due to several factors, including cavity GVD, and the self-phase modulation and nonlinear chirp of the pulses imposed by the dynamical refractive index variation of the III-V gain medium associated with gain depletion and partial gain recovery¹¹.

Current tuning of the MLL: The electrical pumping current of the III-V gain chip (I_{drive}) can serve as an important tuning knob of our MLL. Since I_{drive} can alter the gain spectrum and the refractive index of the gain medium, it can in turn vary the carrier frequency, the coherence property, and the repetition rate (f_{rep}) of the MLL, and potentially lead to locking of the carrier frequency by applying active feedback on I_{drive} . Figure 5 a and b show the dependence of the output spectra and autocorrelation of the MLL on the I_{drive} with 280 mW RF drive fixed at 10.17 GHz. It is evident that within

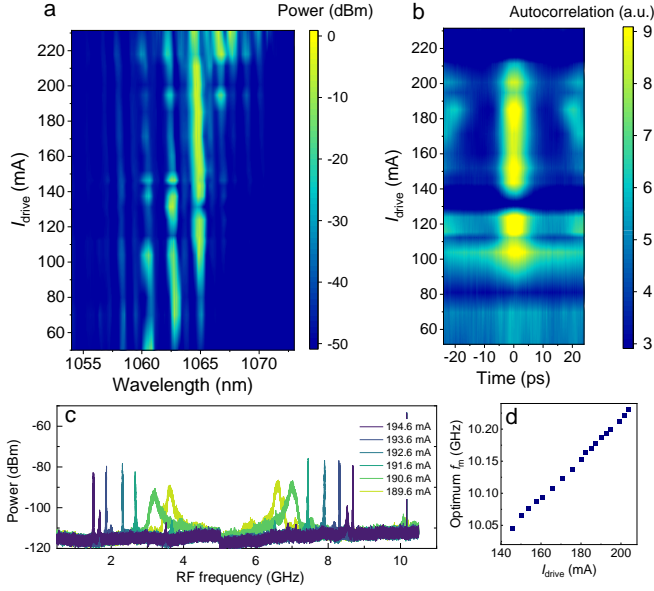


FIG. 5. **Current tuning of integrated actively MLL** **a**, The optical spectrum of the MLL output as a function of the driving current (I_{mod}). **b**, Autocorrelation trace of the MLL output as a function of I_{drive} . In **a** and **b**, the 280 mW RF drive is fixed at 10.17 GHz. **c**, Tuning of the heterodyne beat notes by the I_{drive} . In this measurement, f_m is fixed at 10.18 GHz. **d**, Dependence of optimum f_m for mode-locking on I_{drive} .

a wide range of I_{drive} (140 - 205 mA), optical pulses can be formed inside the laser. In addition, it can be seen in Fig. 5a that the carrier frequency of the MLL blueshifts by ~ 0.3 nm as the I_{drive} is increased from 140 mA to 200 mA. This blueshift, which has also been observed in other reports⁴⁴, is likely caused by the blueshift of the peak wavelength of the gain spectrum due to band filling and screening effects induced by carrier injection⁴⁵.

We then investigated the effect of I_{drive} on the coherence property and the f_{rep} of the laser. We kept the RF drive fixed at 280 mW and 10.18 GHz, and monitored the change in heterodyne beat notes f_1 and f_2 as we slightly varied I_{drive} . The measurement results are summarized in Fig. 5c. As the I_{drive} is tuned from 189.6 mA to 194.6 mA, the laser transitions from the turbulent regime to the mode-locked regime, and then back to the turbulent regime. These results suggest that, with a frequency-stable reference CW laser and active feedback on I_{drive} , it may be possible to lock the carrier frequency of the MLL and operate the device as a stable frequency comb, as the f_{rep} of the MLL has already been locked by the external RF oscillator. As shown in Fig. 5d, when we widely vary I_{drive} from 144 to 204 mA, the optimum f_m that enables mode-locking with high coherence can be varied from 10.04 GHz to 10.23 GHz, indicating the repetition rate of the laser can also be adjusted by ~ 200 MHz by the I_{drive} . Moreover, the optimum f_m increases almost linearly with I_{drive} , which results from an increase of the cavity FSR caused by carrier injection in the gain

medium.

Conclusion and outlook: In summary, we have demonstrated an integrated actively MLL in nanophotonic LN operating around 1065 nm, which can generate ~ 5 ps ultrashort optical pulses. We estimate that the MLL produces an output pulse energy ~ 2.6 pJ and a high peak power greater than 0.5 W, representing the highest pulse energy and peak power of any integrated MLLs in nanophotonic platforms. In contrast to conventional integrated MLLs that integrate both the gain and mode-locking elements on the same III-V chip, our MLL design decouples these elements, resulting in a significantly wider current tuning range and reconfigurability. This, in turn, allows for a wide tuning range of the laser f_{rep} of ~ 200 MHz and precise control of the laser's coherence properties.

Looking forward, the current tuning capability of our MLL indicates that by using a reference and implementing active feedback to the I_{drive} , we can achieve simultaneous locking of the carrier frequency and f_{rep} of the MLL. This allows the MLL to operate as a stable frequency comb with locked carrier frequency offset (f_{CEO}) and f_{rep} . In addition, comprehensive theoretical modeling of the laser dynamics and the identification of the single-pulse operating regime of the laser are of great importance for obtaining even higher peak powers and shorter pulses. We envision that the semiconductor gain and LN nanophotonic mode-locking elements can be fully integrated into the same chip and a better optical coupling between the two platforms can be achieved by adopting an advanced flip-chip bonding process⁴⁶ or heterogeneous integration process^{44,47}. Furthermore, seamless integration of our high peak power MLL with other $\chi^{(2)}$ nonlinear optical functionalities provided by quasi-phase-matched TFLN nanophotonic devices offer exciting opportunities for the development of photonic systems that have yet to be realized in nanophotonics, such as fully integrated supercontinuum sources, self-referenced frequency combs, visible/ultraviolet femtosecond lasers, and atomic clocks.

METHODS

Device fabrication. We fabricated the integrated waveguides, phase modulators, and broadband loop mirrors on a 700-nm-thick X-cut MgO-doped LN thin-film on 4.7- μm -thick SiO_2 on top of a silicon substrate (NANOLN). We first patterned the waveguides using e-beam lithography by employing Hydrogen Silsesquioxane (HSQ) as the e-beam resist. The designed top width of the LN waveguide is 800 nm. The LN layer was etched by 350 nm using Ar^+ plasma. This etching process yields a waveguide sidewall angle of $\sim 60^\circ$. Next, we deposited an 800 nm SiO_2 cladding layer using plasma-enhanced chemical vapor deposition (PECVD). Another e-beam lithography step was used to pattern the RF metal electrodes on top of the cladding layer,

in which PMMA was used as the e-beam resist. Then, we deposited Cr/Au (10 nm/300 nm) using e-beam evaporation. Metal electrodes are formed after metal lift-off in acetone. Finally, the waveguide facets were mechanically polished to enable good light coupling efficiencies.

Optical measurements. For butt coupling the SAF gain chip and the TFLN chip together, the SAF gain chip was placed on a 6-axis nano-positioning stage (Thorlabs) and the TFLN chip was clamped on a fixed sample stage. The two chips could be visually aligned by using a microscope from above. After visual alignment, the alignment was further optimized by maximizing the output power measured by a power meter, which is related to the intra-cavity optical power of the laser. The output power of the MLLs is probed by a single-mode lensed fiber connected to an optical power meter (Thorlabs). The RF drive is provided by an RF signal generator (Rohde & Schwarz SMA100B) and is subsequently amplified by a high-power RF amplifier (Mini-Circuits ZVE-3W-183+). The input RF power is calibrated by an RF power meter (Ladybug). For the results in Fig. 3-5, the laser output spectra were collected by an optical spectrum analyzer (OSA) covering 600-1700 nm (Yokogawa AQ6370B) with a 0.01 nm resolution bandwidth. The RF spectra were collected by an electronic spectrum analyzer (Rohde & Schwarz FSW) with a 100 Hz resolution bandwidth.

Numerical simulations. The optical and RF field distributions shown in Fig. 1a were simulated by COMSOL Multiphysics. We also used commercial software (Lumerical Inc.) to solve for the waveguide modes in order to design the waveguide taper and obtain the dispersion characteristics of the waveguide. In the simulation, the anisotropic index of the LN was modeled by the Sellmeier equations⁴⁸.

DATA AVAILABILITY

The data that support the plots within this paper and other findings of this study are available from the corresponding author upon reasonable request.

CODE AVAILABILITY

The computer code used to perform the nonlinear simulations in this paper is available from the corresponding author upon reasonable request.

ACKNOWLEDGEMENTS

The device nanofabrication was performed at the Kavli Nanoscience Institute (KNI) at Caltech. The au-

thors thank Prof. K. Vahala for loaning equipment. Q.G. thanks Dr. M. Xu for the helpful discussions. The authors gratefully acknowledge support from ARO grant no. W911NF-23-1-0048, NSF grant no. 1846273 and 1918549, AFOSR award FA9550-20-1-0040, and NASA/JPL. The authors wish to thank NTT Research for their financial and technical support.

AUTHORS CONTRIBUTIONS

Q.G. and A.M. conceived the project; Q.G. fabricated the devices with assistance from R.S.. Q.G. performed the measurements, numerical simulation, and analyzed the data. R.S., J.W., B.G., R.M.G., L.L., L.C., and S.Z. assisted with the measurements. B.G., A.R., and M. L. helped with the numerical simulation and data analysis. Q.G. wrote the manuscript with inputs from all authors. A.M. supervised the project.

COMPETING INTERESTS

Q.G. and A.M. are inventors on a patent application (US patent application no. 17/500,425) that covers the concept and implementation of the actively mode-locked laser here. The remaining authors declare no competing interests.

- [1] M. Wegener, *Extreme nonlinear optics: an introduction* (Springer Science & Business Media, 2005).
- [2] A. H. Zewail, The Journal of Physical Chemistry A **104**, 5660 (2000).
- [3] J. M. Dudley, G. Genty, and S. Coen, Reviews of Modern Physics **78**, 1135 (2006).
- [4] S. A. Diddams, T. Udem, J. Bergquist, E. Curtis, R. Drullinger, L. Hollberg, W. M. Itano, W. Lee, C. Oates, K. Vogel, *et al.*, Science **293**, 825 (2001).
- [5] A. D. Ludlow, M. M. Boyd, J. Ye, E. Peik, and P. O. Schmidt, Reviews of Modern Physics **87**, 637 (2015).
- [6] T. Udem, R. Holzwarth, and T. W. Hänsch, Nature **416**, 233 (2002).
- [7] D. W. Piston, Trends in cell biology **9**, 66 (1999).
- [8] N. G. Horton, K. Wang, D. Kobat, C. G. Clark, F. W. Wise, C. B. Schaffer, and C. Xu, Nature Photonics **7**, 205 (2013).
- [9] A. Marandi, Z. Wang, K. Takata, R. L. Byer, and Y. Yamamoto, Nature Photonics **8**, 937 (2014).
- [10] M. L. Davenport, S. Liu, and J. E. Bowers, Photonics Research **6**, 468 (2018).
- [11] P. J. Delfyett, L. T. Florez, N. Stoffel, T. Gmitter, N. C. Andreadakis, Y. Silberberg, J. P. Heritage, and G. A. Alphonse, IEEE Journal of Quantum Electronics **28**, 2203 (1992).
- [12] A. Hermans, K. Van Gasse, J. Ø. Kjellman, C. Caër, T. Nakamura, Y. Inada, K. Hisada, T. Hirasawa, S. Cuyvers, S. Kumari, *et al.*, APL Photonics **6**, 096102 (2021).
- [13] E. Vissers, S. Poelman, H. Wenzel, H. Christopher, K. Van Gasse, A. Knigge, and B. Kuyken, Optics Express **30**, 42394 (2022).
- [14] A. Bhardwaj, R. Bustos-Ramirez, G. E. Hoeffler, A. Dentai, M. E. Plascak, F. Kish, P. J. Delfyett, and M. C. Wu, IEEE Journal of Quantum Electronics **56**, 1 (2020).
- [15] C. Wang, M. Zhang, X. Chen, M. Bertrand, A. Shams-Ansari, S. Chandrasekhar, P. Winzer, and M. Lončar, Nature **562**, 101 (2018).
- [16] M. Xu, Y. Zhu, F. Pittalà, J. Tang, M. He, W. C. Ng, J. Wang, Z. Ruan, X. Tang, M. Kuschnerov, *et al.*, Optica **9**, 61 (2022).
- [17] C. Wang, C. Langrock, A. Marandi, M. Jankowski, M. Zhang, B. Desiatov, M. M. Fejer, and M. Lončar, Optica **5**, 1438 (2018).
- [18] J. Lu, J. B. Surya, X. Liu, A. W. Bruch, Z. Gong, Y. Xu, and H. X. Tang, Optica **6**, 1455 (2019).
- [19] M. Jankowski, C. Langrock, B. Desiatov, A. Marandi, C. Wang, M. Zhang, C. R. Phillips, M. Lončar, and M. M. Fejer, Optica **7**, 40 (2020).
- [20] L. Ledezma, A. Roy, L. Costa, R. Sekine, R. Gray, Q. Guo, R. M. Briggs, and A. Marandi, arXiv preprint arXiv:2203.11482 (2022).
- [21] J. Lu, A. Al Sayem, Z. Gong, J. B. Surya, C.-L. Zou, and H. X. Tang, Optica **8**, 539 (2021).
- [22] T. P. McKenna, H. S. Stokowski, V. Ansari, J. Mishra, M. Jankowski, C. J. Sarabalis, J. F. Herrmann, C. Langrock, M. M. Fejer, and A. H. Safavi-Naeini, Nature Communications **13**, 4532 (2022).
- [23] A. Roy, L. Ledezma, L. Costa, R. Gray, R. Sekine, Q. Guo, M. Liu, R. M. Briggs, and A. Marandi, arXiv preprint arXiv:2212.08723 (2022).
- [24] A. Roy, R. Nehra, S. Jahani, L. Ledezma, C. Langrock, M. Fejer, and A. Marandi, Nature Photonics **16**, 162 (2022).
- [25] Q. Guo, R. Sekine, L. Ledezma, R. Nehra, D. J. Dean, A. Roy, R. M. Gray, S. Jahani, and A. Marandi, Nature Photonics **16**, 625 (2022).
- [26] R. Nehra, R. Sekine, L. Ledezma, Q. Guo, R. M. Gray, A. Roy, and A. Marandi, Science **377**, 1333 (2022).
- [27] Z. Gong, X. Liu, Y. Xu, M. Xu, J. B. Surya, J. Lu, A. Bruch, C. Zou, and H. X. Tang, Optics Letters **44**, 3182 (2019).
- [28] Y. He, Q.-F. Yang, J. Ling, R. Luo, H. Liang, M. Li, B. Shen, H. Wang, K. Vahala, and Q. Lin, Optica **6**, 1138 (2019).
- [29] M. Zhang, B. Buscaino, C. Wang, A. Shams-Ansari, C. Reimer, R. Zhu, J. M. Kahn, and M. Lončar, Nature **568**, 373 (2019).
- [30] Y. Hu, M. Yu, B. Buscaino, N. Sinclair, D. Zhu, R. Cheng, A. Shams-Ansari, L. Shao, M. Zhang, J. M. Kahn, *et al.*, Nature Photonics **16**, 679 (2022).
- [31] M. Yu, D. Barton III, R. Cheng, C. Reimer, P. Kharel, L. He, L. Shao, D. Zhu, Y. Hu, H. R. Grant, *et al.*, Nature, 1 (2022).
- [32] D. Kuizenga and A. Siegman, IEEE Journal of Quantum Electronics **6**, 694 (1970).
- [33] R. Nagar, D. Abraham, and G. Eisenstein, Optics Letters **17**, 1119 (1992).
- [34] A. Rueda, F. Sedlmeir, M. Kumari, G. Leuchs, and H. G. Schwefel, Nature **568**, 378 (2019).
- [35] J. P. Salvestrini, L. Guilbert, M. Fontana, M. Abarkan, and S. Gille, Journal of Lightwave Technology **29**, 1522 (2011).
- [36] A. M. Perego, B. Garbin, F. Gustave, S. Barland, F. Prati, and G. J. De Valcárcel, Nature Communications **11**, 311 (2020).
- [37] I. N. Duling III, *Compact sources of ultrashort pulses* (1995).
- [38] M. Jin, J. Chen, Y. Sua, P. Kumar, and Y. Huang, Optics Letters **46**, 1884 (2021).
- [39] T. Mitarai, E. Moataz, T. Miyazaki, T. Amemiya, and N. Nishiyama, Japanese Journal of Applied Physics **59**, 112002 (2020).
- [40] E. Vissers, S. Poelman, C. O. de Beeck, K. Van Gasse, and B. Kuyken, Optics Express **29**, 15013 (2021).
- [41] F. Kärtner, D. Zumbühl, and N. Matuschek, Physical Review Letters **82**, 4428 (1999).
- [42] A. E. Siegman, *Lasers* (University science books, 1986).
- [43] H. A. Haus, IEEE Journal of Selected Topics in Quantum Electronics **6**, 1173 (2000).
- [44] C. O. de Beeck, F. M. Mayor, S. Cuyvers, S. Poelman, J. F. Herrmann, O. Atalar, T. P. McKenna, B. Haq, W. Jiang, J. D. Witmer, *et al.*, Optica **8**, 1288 (2021).
- [45] S. Schmitt-Rink, D. Chemla, and D. A. Miller, Physical Review B **32**, 6601 (1985).
- [46] A. Shams-Ansari, D. Renaud, R. Cheng, L. Shao, L. He, D. Zhu, M. Yu, H. R. Grant, L. Johansson, M. Zhang, *et al.*, Optica **9**, 408 (2022).
- [47] X. Zhang, X. Liu, L. Liu, Y. Han, H. Tan, L. Liu, Z. Lin, S. Yu, R. Wang, and X. Cai, Applied Physics Letters **122** (2023).

- [48] D. E. Zelmon, D. L. Small, and D. Jundt, JOSA B **14**, 3319 (1997).